

## Coster-Kronig yields of the $_{54}\text{Xe}$ $L$ subshells measured through synchrotron photoionization

W. Jitschin and R. Stötzel

*Fachbereich Mathematik, Naturwissenschaften und Informatik, Fachhochschule Giessen-Friedberg, 35390 Giessen, Germany*

T. Papp

*Institute of Nuclear Research, Hungarian Academy of Science, P.O. Box 51, 4001 Debrecen, Hungary*

M. Sarkar

*Saha Institute of Nuclear Physics, Calcutta 700064, India*

G. D. Doolen

*Los Alamos National Laboratory, Los Alamos, New Mexico 87545*

(Received 24 October 1994)

The method of selective photoionization of individual subshells by monochromatized synchrotron radiation has been employed to measure all Coster-Kronig yields of the  $_{54}\text{Xe}$   $L$  subshells. The energy of the primary radiation was set at about 50 energy points in the range of the  $L$  edges. At each setting, the induced Xe  $L$  fluorescence and the induced Ar  $K$  fluorescence (used for normalization purposes) were recorded simultaneously by a Si(Li) detector. Both Xe and Ar were in the gaseous state. The recorded fluorescence spectra were carefully analyzed with proper modeling of the line tailing due to the intrinsic line profile and the detector line shape. The Coster-Kronig yields were derived by fitting the measured fluorescence intensities versus primary energy with the photoelectric cross sections. The derived yields are sensitive to the precise dependence of the cross sections on primary energy. Evaluations have been performed assuming a smooth power-law dependence and employing corrections for electron-correlation effects, which were estimated from comparative calculations in the independent-particle approximation and linear-response approximation models. Still, the uncertainties of the correlation effects constitute the main contribution to the uncertainties of the derived Coster-Kronig yields. The finally adopted values are  $f_{12} = 0.12 \pm 0.03$ ,  $f_{13} = 0.23 \pm 0.04$ , and  $f_{23} = 0.14 \pm 0.02$ .

PACS number(s): 32.30.Rj, 32.80.Fb, 32.70.Jz, 32.80.Hd

### I. INTRODUCTION

A vacancy in an atomic inner shell rapidly decays through a cascade of transitions, most of which are radiationless. Fastest among these processes are the Coster-Kronig transitions, i.e., radiationless transitions from a deeper subshell to a less tightly bound subshell of the same shell.

Coster-Kronig transitions are of relevance both in fundamental atomic physics and in experimental applications. The large transition rates may stretch perturbation approaches to their limits, and the onset of allowed transition channels is very sensitive to the dynamical response of the residual electrons. Quantitative analytical work requires accurate knowledge of Coster-Kronig yields, since these transitions redistribute vacancies within one shell, and thus directly affect the intensities of emission lines.

Comprehensive theoretical calculations of radiative and radiationless inner-shell decay rates are available [1,2]. In the case of radiationless transitions with small excess energies, calculated yields bear substantial uncertainty due to the problem of predicting the exact atomic number at which the onset of an allowed decay channel occurs [3].

Various experimental methods have been applied to measure the decay yields [4]. Most of these methods rely

on the availability of proper radioactive nuclides and suffer from various experimental problems. Experimental data still are scarce [5]. There are some accurate and reliable measurements on medium- and high- $Z$  atoms [6]. A powerful method for measuring the Coster-Kronig yield  $f_{23}$  (as well as the fluorescence yields  $\omega_2$  and  $\omega_3$ ) is the  $K\alpha$ - $L\alpha$  coincidence method. This method has reached a state of maturity at which systematic errors have been carefully analyzed. Recent progress comprises multiparameter data acquisition [7] and advanced modeling of detector tailing in the fluorescence analysis [8]. Unfortunately, the  $K\alpha$ - $L\alpha$  method cannot be applied to investigate the decay of the  $L_1$  subshell (e.g., the Coster-Kronig yields  $f_{12}$  and  $f_{13}$ ) because there is no strong  $K$ - $L_1$  radiative transition.

About a decade ago, a novel method of measuring all yields was introduced which relies on subshell-selective photoionization [9]. In this method, monochromatized synchrotron radiation is tuned over the  $L$  subshell absorption edges and ionizes only the  $L_3$ , both the  $L_3$  and  $L_2$ , or all three  $L$  subshells. By recording the induced x-ray fluorescence or the Auger emission one can determine all Coster-Kronig yields. In particular, fluorescence measurements give good results [10–12], whereas the Auger-emission experiments suffer both from the inherent complexity of the Auger spectrum as well as the small signal

strength obtained with present second-generation synchrotron sources [13–15]. Normalization of the fluorescence intensity to the varying primary intensity can reliably be performed by recording simultaneously the  $K$  fluorescence of a properly chosen element.

Applying this method, it has been found that the photoelectric cross sections of the  $L$  subshells exhibit a more complex dependence on photon energy than predicted from standard single-electron calculations [16]. This behavior is due to electron-correlation effects and has to be taken into account in order to derive reliable Coster-Kronig yields.

Comprehensive experimental data of Coster-Kronig yields are available for high- $Z$  elements, whereas the situation is still unsettled in the case of medium- $Z$  and small- $Z$  elements [6]. In the present paper we report on a recent measurement of the Coster-Kronig yields of Xe. Some aspects of the applied method and the experiment are not discussed here since they have already been addressed in an earlier comprehensive paper [12].

## II. EXPERIMENTAL DETAILS

The measurements were performed at the x-ray beam line of the ELSA storage ring at the Physikalisches Institut, Universität Bonn, Germany. The primary radiation was monochromatized by a double-crystal monochromator. In contrast to previous work, a gaseous sample was used. For this purpose, a gas chamber of length 134 mm equipped with thin windows (10- $\mu\text{m}$  polyethylene terephthalat, called hostaphane<sup>®</sup>) was inserted into the primary beam. The chamber was first evacuated, then filled with 20 mbar Ar and finally 20 mbar Xe were added. The pressures were measured with a capacitance diaphragm gauge. After filling, the chamber was valved off, leading to a constant amount of gas during the measurements. The induced fluorescence passed through another thin window of the chamber and was detected at right angles to the primary beam. The detector model was PGT Type 321 with a specified resolution of 160 eV full width at half maximum (FWHM) at 5.9 keV.

The fluorescence intensity obtained was large. In order to avoid significant pileup effects in the detector, the counting rate was kept below  $1000 \text{ s}^{-1}$  by using narrow slits for the incoming radiation. The recording time of a single fluorescence spectrum was 10–15 min. The area of the Xe  $L\alpha$  line typically contained  $10^5$  total counts, providing good statistics. All together, 51 usable spectra were recorded at different primary energies in the range of the Xe  $L$  edges (Fig. 1).

The energy of the primary radiation is known from the monochromator setting. It can be independently checked from the measured fluorescence spectra which exhibit a small line of coherently scattered primary photons (see Fig. 1). In fitting the spectra (see below), the energy scale is calibrated using tabulated Xe emission energies. The fitted position of the scattered photons line then gives the primary energy. Agreement between selected and fitted energies was within  $\pm 9 \text{ eV}$ , i.e., very good, except for a few apparent errors.

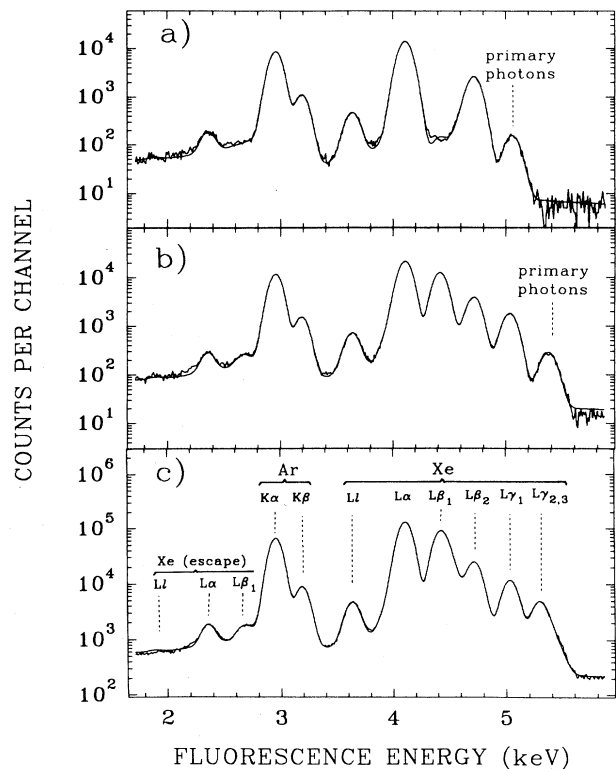


FIG. 1. Ar  $K$  and Xe  $L$  fluorescence spectra excited by primary photons at various energies. Experimental data are represented by the noisy curves. Fitted spectra are represented by the smooth curves. All spectra show the Ar  $K$  fluorescence. (a) Additionally Xe  $L_3$  fluorescence excited, (b) Xe  $L_3$  and  $L_2$  fluorescence excited, (c) Xe  $L_3$ ,  $L_2$ , and  $L_1$  fluorescence excited.

## III. LINE FITTING OF FLUORESCENCE SPECTRA

The measured spectra consist of the Ar  $K$  and Xe  $L$  lines as well as coherently scattered primary radiation. The strongest lines are resolved, but there are numerous additional lines (Table I). In order to perform a physically meaningful fit, all lines have to be considered. This was achieved by fitting the stronger lines individually (relative intensities given as “1.0000” in Table I), and by “locking” a weaker line to a stronger line that originates from the same subshell and lies close in energy (i.e., a preceding line in Table I). The energies of all lines were taken from a tabulation (except for the primary radiation) [17]. The relative intensity of a weak line (i.e., its intensity related to that of the corresponding strong line) was taken from theoretical calculations [1,18] and corrected for the detector efficiency.

Great effort was spent on the fitting of the recorded fluorescence spectra. The actual shape of a recorded line is a convolution of a Lorentzian profile (due to the lifetime of the involved states) and a Gaussian profile with additional low-energy tail (due to the detector characteristics). The widths of individual states were taken from the literature [19]. Although in the present case the

TABLE I. Compilation of lines and parameters used in the fits of the fluorescence spectra (see text).

Transition	Line	Energy (keV)	Linewidth (eV)	Relative intensity
Ar	$K-L_{2,3}$	$K\alpha$	2.957	1.0000
	$K-M$	$K\beta$	3.190	1.0000
Xe	$L_3-M_1$	$Ll$	3.637	13.36
	$L_3-M_5$	$L\alpha_1$	4.110	3.44
	$L_3-M_4$	$L\alpha_2$	4.097	3.52
	$L_3-N_{4,5}$	$L\beta_{2,15}$	4.719	3.10
	$L_3-N_1$	$L\beta_6$	4.574	0.0520
	$L_3-O_1$	$L\beta_7$	4.764	0.0085
Xe	$L_2-M_1$	$L\eta$	3.958	11.47
	$L_2-M_4$	$L\beta_1$	4.418	3.41
	$L_2-N_4$	$L\gamma_1$	5.037	2.95
	$L_2-N_1$	$L\gamma_5$	4.894	0.0390
	$L_2-O_1$	$L\gamma_8$	5.084	0.0060
Xe	$L_1-M_3$	$L\beta_3$	4.512	7.43
	$L_1-M_2$	$L\beta_4$	4.452	6.00
	$L_1-M_{4,5}$	$L\beta_{9,10}$	4.770	0.0235
	$L_1-N_{2,3}$	$L\gamma_{2,3}$	5.307	3.7
	$L_1-N_{2,3}$	$L\gamma_{2,3}$	5.250	0.1700
	$L_1-N_{2,3}$	$L\gamma_{2,3}$	5.275	0.1700
	$L_1-N_{4,5}$	$L\gamma_{11}$	5.384	0.0080
	$L_1-O_{2,3}$	$L\gamma_{4,4'}$	5.440	0.1330
Primary radiation		variable		1.0000

Lorentzian width is always much smaller than the Gaussian width, the Lorentzian profile has substantial influence on the line wings. Furthermore, the detector causes artificial asymmetric low-energy tails and escape lines (Si  $K\alpha$ , i.e., 1.740 keV below the main line) for each line.

The recorded spectra were fitted using the code GPP [20] which recently was carefully examined [8]. The line

shape was represented as a convolution of intrinsic Lorentzian shape and detector profile. The tailing of the detector was carefully determined at various resolved fluorescence lines, i.e., at the Ar  $K\alpha$  line, at the Xe  $Ll, L\alpha$  lines and at the Xe  $L\beta$  group. The sophisticated modeling of the detector line shape allowed very exact fits of the recorded fluorescence spectra (see Fig. 1). Thus it was possible to perform independent fits even of weak lines which are completely buried under strong lines. An example is the weak  $L\eta$  line. The constant  $L\eta$  to  $L\beta_1$  ratio obtained is a remarkably excellent result.

Problems were encountered while attempting to fit the Xe  $L\gamma_{23}$  line either as a single line with 6–9 eV Lorentzian width [21,22] or as a doublet with known relative intensities [1] (Fig. 2, left). In fact, high-resolution measurements [23] have revealed that the Xe  $L\gamma_{23}$  line has a complex shape caused by the breakdown of the quasiparticle picture of a  $4p$  hole due to strong dynamical correlations [19]. When the actual shape of the Xe  $L\gamma_{23}$  line was approximated by the three individual lines as given in Table I, good fits were obtained (Fig. 2, right).

For the extraction of the Coster-Kronig yields, only the intensities of the strongest lines are required, i.e., one line originating from the Xe  $L_3$  subshell, one line originating from the Xe  $L_2$  subshell, and the Ar  $K\alpha$  line for normalization. The obtained Xe  $L\alpha$  to Ar  $K\alpha$  and Xe  $L\beta_1$  to Ar  $K\alpha$  intensity ratios as functions of primary photon energy are displayed in Fig. 3.

#### IV. DETERMINATION OF COSTER-KRONIG YIELDS

The procedure of extracting Coster-Kronig yields in the synchrotron photoionization methods has been exten-

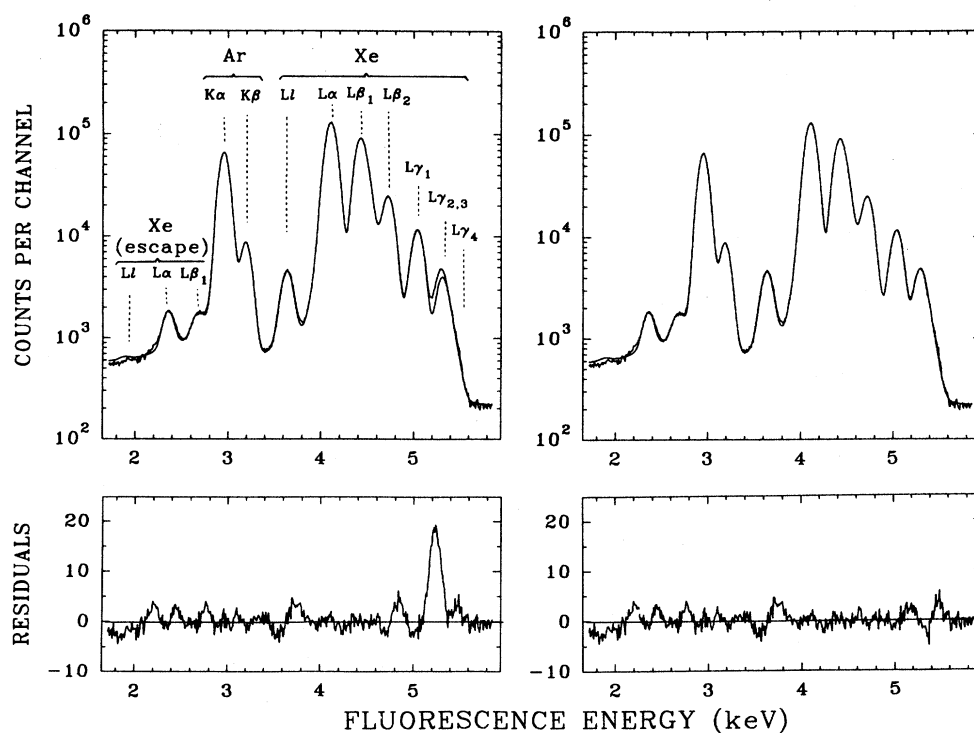


FIG. 2. Fit of the fluorescence spectrum of Fig. 1(c). Left: assuming the  $L\gamma_{2,3}$  line is a single line at 5.307 keV [23]. Right: assuming the  $L\gamma_{2,3}$  line as the composite line given in Table I.

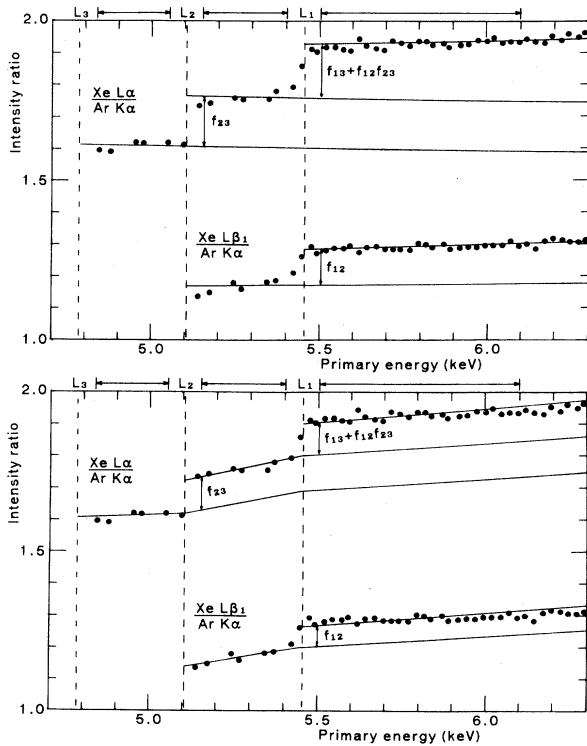


Fig. 3. Xe  $L\alpha$  to Ar  $K\alpha$  and Xe  $L\beta_1$  to Ar  $K\alpha$  intensity ratios vs energy of the primary photons. Points are experimental data. Curves are the fitted results using photoelectric cross sections. The energy intervals included in the fits are indicated. Top: Cross sections without corrections for electron correlations. Bottom: Cross sections with corrections for electron correlations.

sively discussed in previous papers [10,12]. Briefly, the intensities of the Xe  $L\alpha$  line (strongest line originating from the  $L_3$  level) and the  $L\beta_1$  line (strongest line from  $L_2$ ) normalized to the intensity of the Ar  $K\alpha$  line are given by

$$\frac{I(\text{Xe } L\alpha)}{I(\text{Ar } K\alpha)} = \text{const} \times \left[ \frac{\sigma_{L_3}}{\sigma_K} + f_{23} \frac{\sigma_{L_2}}{\sigma_K} + (f_{13} + f_{12}f_{23}) \frac{\sigma_{L_1}}{\sigma_K} \right], \quad (1)$$

$$\frac{I(\text{Xe } L\beta_1)}{I(\text{Ar } K\alpha)} = \text{const}' \times \left[ \frac{\sigma_{L_2}}{\sigma_K} + f_{12} \frac{\sigma_{L_1}}{\sigma_K} \right], \quad (2)$$

where const and const' are constants in the experiment and  $\sigma_K$ ,  $\sigma_{L_3}$ ,  $\sigma_{L_2}$ , and  $\sigma_{L_1}$  are the photoelectric cross sections of the indicated Ar  $K$  shell or Xe  $L$  subshells. Since the photoelectric cross sections are zero below the corresponding edge, the intensity jumps of the Xe  $L\alpha$  and  $L\beta_1$  lines at the edges correspond to a vacancy transfer from a deeper-lying subshell to a higher one. The relative size of a particular jump is a measure for the corresponding Coster-Kronig yield (Fig. 3).

For the extraction of Coster-Kronig yields one must

use the photoelectric cross sections. In the following, a simple approach to the cross sections is chosen first, and then, a more realistic one.

As is very generally assumed, the photoelectric cross section varies smoothly with primary energy (except at the thresholds). Within a reasonable energy range it can be well described by a power-law dependence on the energy  $E$ . This description leads to a good reproduction of the body of experimental data [24]. It is also supported by standard theoretical calculations within the single-electron model. We follow this practice using the ansatz

$$\sigma_i = \begin{cases} 0 & \text{below the edge} \\ [a_i(\text{Mb})] \times [E(\text{keV})]^{b_i} & \text{above the edge} \end{cases}, \quad (3)$$

where  $a_i$  and  $b_i$  are constants for a particular (sub)shell  $i$ . In order to determine these constants, we have adopted the numerical results of theoretical calculations [25]. These provide consistent results and—for our case—agree with experiment within a few percent on an absolute scale [24]. The fitted constants are given in Table II. Tabulated constants derived from the experimental data have similar values [26].

Once the photoelectric cross sections are known as functions of energy, a comparison of the experimentally obtained normalized line intensities (Fig. 3) with the cross sections [Eq. (3)] directly provides the three Coster-Kronig yields  $f_{23}$ ,  $f_{12}$ , and  $f_{13}$  [Eqs. (1) and (2)]. In the procedure of the comparison, data within  $\pm 50$  eV of an edge were omitted since they may be affected by near-edge structure, e.g., due to two-electron processes [27,28] as well as electron-correlation effects (see below). We note that in the fit procedure only the heights of the lines (Fig. 3) are adjusted, whereas the slope is fixed by the adopted energy dependence of the cross sections. For illustration, the fitted results are shown at the top of Fig. 2.

As can be seen, the fit gives a reasonable overall reproduction of the measured intensity ratios, but systematic deviations can also be recognized. In particular, the experimental data show a slight increase between the  $L_3$  and  $L_2$  edge and a substantial increase between the  $L_2$  and  $L_1$  edge, which is not reproduced by the ansatz.

These minor deviations from a power-law ansatz in the range of the  $L$  edges are caused by electron-correlation effects, as is now well established both experimentally and theoretically [16]. The electron correlations change the slope of the cross sections (in particular between the  $L_2$  and  $L_1$  edges) and cause dispersionlike features in the vicinity of the edges. They can be treated theoretically within the relativistic time-dependent local-density ap-

TABLE II. Coefficients obtained in an analytical fit to the photoelectric cross sections [see Eq. (3)].

Element	(Sub)shell	$a_i$	$b_i$
Ar	$K$	1.860	-2.676
Xe	$L_3$	7.818	-2.753
Xe	$L_2$	3.716	-2.654
Xe	$L_1$	0.467	-1.765

TABLE III. Obtained Coster-Kronig yields.

	Present work			Ref. [32] $K\alpha$ - $L\alpha$ coincidence	Ref. [5] semiempirical	Ref. [3] Relativistic theory
	Fit without correlation	Fit with correlation	Adopted value			
$f_{12}$	0.169	0.095	$0.12 \pm 0.03$		$0.19 \pm 0.04$	0.196
$f_{13}$	0.316	0.185	$0.23 \pm 0.04$		$0.28 \pm 0.04$	0.328
$f_{23}$	0.174	0.115	$0.14 \pm 0.02$	$0.148 \pm 0.029$	$0.154 \pm 0.03$	0.174

proximation; their size can be obtained by comparing calculations omitting the correlations [independent particle approximation (IPA)] and including the correlations [linear response approximation (LRA)] [29–31]. These effects can also be directly seen in experimental x-ray mass attenuation scans (Ref. [16] for heavier elements, our own unpublished results for  $_{51}\text{Sb}$ ).

Detailed comparative IPA-LRA calculations of subshell cross sections are available for  $_{47}\text{Ag}$  and  $_{62}\text{Sm}$  (Fig.

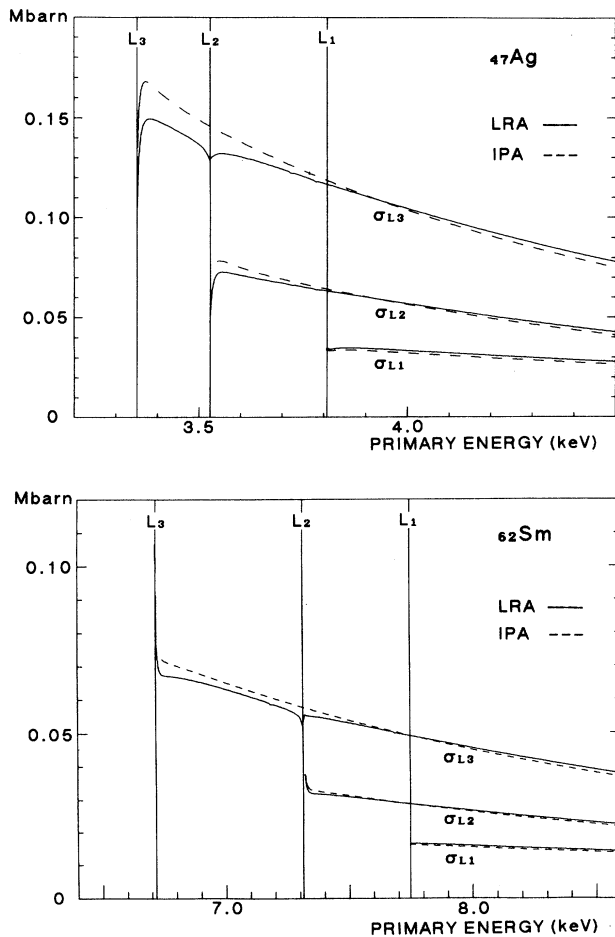


FIG. 4. Photoelectric cross section of the individual  $L$  subshells calculated with omission (IPA, independent-particle approximation) and inclusion (LRA, linear-response approximation) of electron correlations. Top:  $_{47}\text{Ag}$ ; bottom:  $_{62}\text{Sm}$ .

4). Since  $_{54}\text{Xe}$  has nearly the mean atomic number of these two elements, we estimated the influence of correlation effects on the photoelectric cross sections by interpolation. If cross-section data from the vicinities of the edges are omitted, it is reasonable to make a linear approximation for each range between two particular edges. Furthermore, the relative influence is assumed to be equal for each individual  $L$  subshell as is approximately predicted by theory. Thus, by comparing the IPA and LRA calculations, the following changes in the photoelectric cross sections due to correlation effects were estimated:  $-6.6\%$  at  $L_3$  edge (4.782 keV),  $-5.6\%$  at  $L_2$  edge (5.104 keV),  $-0.9\%$  at  $L_1$  edge (5.453 keV), and  $+2.4\%$  at 6.100 keV.

As the best estimates of the actual photoelectric cross sections, the values calculated with the previous power-law ansatz with corrections for the electron-correlation effects were adopted. Taking these cross sections, new fits to the experimental intensity data were performed. The results are displayed at the bottom of Fig. 3.

The agreement between fitted results and experimental data improved compared with the previous fit (Fig. 3 top), both in the ranges between the  $L_3$  and  $L_2$  edges and between the  $L_2$  and  $L_1$  edges. However, agreement became somewhat worse above the  $L_1$  edge where the experimental data exhibit a smaller slope than the assumed cross sections.

In order to check the reliability of the data fitting, additional fits using the second strongest  $L_3$  and  $L_2$  lines instead of the strongest lines were performed using  $L\beta_2$  and  $L\gamma_1$  instead of  $L\alpha$  and  $L\beta_1$ , respectively, in Eqs. (1) and (2). The Coster-Kronig yields obtained are very similar; their weighted averages are given in the second and third columns of Table III (labeled “without correlation” and “with correlations”).

As can be seen from Fig. 3, the two fits including or omitting the electron-correlation effects both give a rather reasonable description of the experimental data. However, the inclusion of correlation effects results in substantially smaller jumps at the edges and thus substantially smaller Coster-Kronig yields. The most crucial point for the derived yields is the energy dependence (slope) of the cross sections in the range between the  $L_2$  and  $L_1$  subshells. The first fit (with small slope) must be regarded as unrealistic since it simply ignores the established correlation effects. The second fit (with large slope) includes these effects, but the assumed size of the correlation effects depends on the arbitrary interpolation of somewhat unreliable calculations. Figure 3 indicates that these effects are slightly overestimated (at least above the

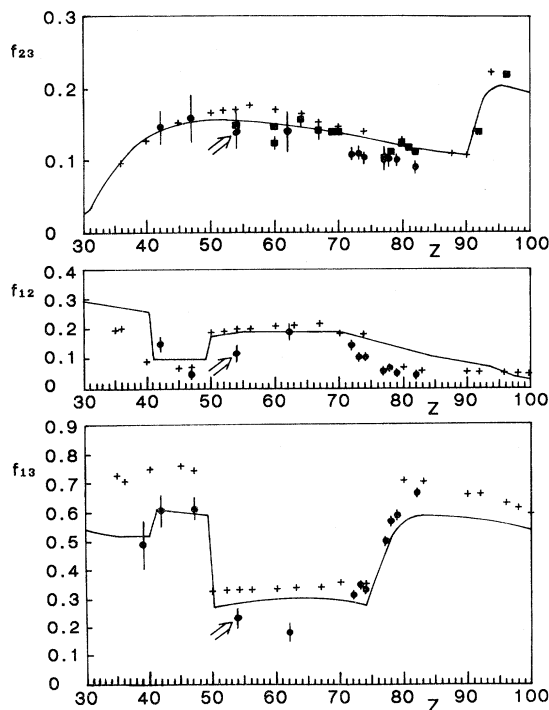


FIG. 5. Coster-Kronig yields vs atomic number. Dots are experimental results by the synchrotron photoionization method (present work indicated by arrows). Squares are experimental results by the  $K\alpha$ - $L\alpha$  coincidence method. Crosses are theoretical results [3]. Curve is a semiempirical fit [5].

$L_1$  edge). Dedicated x-ray mass attenuation studies might determine the exact size of these effects. As final results of the Coster-Kronig yields a weighted average ( $\frac{1}{3}$  first fit,  $\frac{2}{3}$  second fit) was adopted (fourth column of Table III; Fig. 5).

## V. DISCUSSION AND CONCLUSION

The method of subshell-selective photoionization has been applied to measure all  $L$  subshell Coster-Kronig yields of Xe; the induced  $L$  fluorescence has been recorded at various primary energies. The present measurement is an explorative extension of previous comprehensive measurements towards elements with lower atomic numbers. It turns out that these elements are accessible by the method, but great care has to be taken in utilizing the proper photoelectric cross sections. The cross sections exhibit characteristic features in the range of the  $L$  edges caused by electron correlations which are almost negligible for heavy elements but increase with decreasing  $Z$  and become substantial for medium- $Z$  elements. In the present work, the uncertainties in the photoelectric cross sections are the main source of uncertainty for the derived Coster-Kronig yields.

The Coster-Kronig yields of  $^{54}\text{Xe}$  obtained here can be compared with other experimental and theoretical values (Fig. 5). They fit well the general trend of previous measurements for other elements using the same method. There is one measurement of the  $f_{23}$  yield of  $^{54}\text{Xe}$  by the  $K\alpha$ - $L\alpha$  coincidence method [32]. The  $f_{23}$  yield of the present work is compatible with but slightly smaller than that obtained by the coincidence method. This behavior has been observed previously for heavier elements. All Coster-Kronig yields obtained in the present work are smaller than theoretical predictions and the semiempirical curve (which for medium- $Z$  elements is mainly based on theory). Again, such a deviation is in accord with previous experimental work.

## ACKNOWLEDGMENTS

The experiment was made possible by the courtesy of Professor Dr. J. Hormes. The valuable contributions of W. Schmidt and J. Doppelfeld to the measurements are gratefully acknowledged.

- [1] J. H. Scofield, Phys. Rev. A **10**, 1507 (1974); At. Data Nucl. Data Tables **14**, 121 (1974).
- [2] M. H. Chen, B. Crasemann, and H. Mark, At. Data Nucl. Data Tables **24**, 13 (1979).
- [3] M. H. Chen, B. Crasemann, and H. Mark, Phys. Rev. A **24**, 117 (1981).
- [4] W. Bambynek, B. Crasemann, R.W. Fink, H.-U. Freund, H. Mark, C. D. Swift, R. E. Price, and P. V. Rao, Rev. Mod. Phys. **44**, 716 (1972).
- [5] M. O. Krause, J. Phys. Chem. Ref. Data **8**, 307 (1979).
- [6] W. Jitschin, in *X-ray and Inner-shell Processes*, edited by T. A. Carlson, M. O. Krause, and S. T. Manson, AIP Conf. Proc. No. **215** (AIP, New York, 1990).
- [7] P. L. McGhee and J. L. Campbell, J. Phys. B **21**, 2295 (1988).
- [8] T. Papp, J. L. Campbell, and S. Raman, Phys. Rev. A **49**, 729 (1994).
- [9] W. Jitschin, G. Materlik, U. Werner, and P. Funke, J. Phys. B **18**, 1139 (1985).
- [10] U. Werner and W. Jitschin, Phys. Rev. A **38**, 4009 (1988).
- [11] R. Stötzel, U. Werner, M. Sarkar, and W. Jitschin, Phys. Rev. A **45**, 2093 (1992).
- [12] R. Stötzel, U. Werner, M. Sarkar, and W. Jitschin, J. Phys. B **25**, 2295 (1992).
- [13] W. Jitschin, G. Grosse, and P. Röhl, Phys. Rev. A **39**, 103 (1989).
- [14] S. L. Sorenson, R. Carr, S. J. Schaphorst, S. B. Whitfield, and B. Crasemann, Phys. Rev. A **39**, 6241 (1989).
- [15] S. L. Sorenson, S. J. Schaphorst, S. B. Whitfield, and B. Crasemann, Phys. Rev. A **44**, 350 (1991).
- [16] W. Jitschin, U. Werner, G. Materlik, and G. D. Doolen, Phys. Rev. A **35**, 5038 (1987).
- [17] K. D. Sevier, At. Data Nucl. Data Tables **24**, 323 (1979).
- [18] J. L. Campbell and J.-X. Wang, At. Data Nucl. Data Tables **43**, 281 (1989).
- [19] M. Ohno and R. E. LaVilla, Phys. Rev. A **45**, 4713 (1992).
- [20] J. L. Campbell and W. J. Teesdale, Nucl. Instrum. Methods Phys. Res. Sect. B **43**, 218 (1989).
- [21] O. Keski-Rahkonen and M. O. Krause, At. Data Nucl. Data Tables **14**, 139 (1974).

- [22] S. I. Salem and P. L. Lee, *At. Data Nucl. Data Tables* **18**, 233 (1976).
- [23] M. Ohno and R. E. LaVilla, *Phys. Rev. A* **38**, 3479 (1988).
- [24] E. B. Saloman, J. H. Hubbell, and J. H. Scofield, *At. Data Nucl. Data Tables* **38**, 1 (1988).
- [25] J. H. Scofield, Lawrence Livermore Radiation Laboratory Report No. UCRL-51326, 1973 (unpublished).
- [26] E. Preuß, Kernforschungsanlage (KFA)-Jülich Report No. Jül-856-TP, 1972 (unpublished).
- [27] KeZhang, E. A. Stern, and J. J. Rehr, in *EXAFS and Near Edge Structure III*, edited by K. O. Hodgson, B. Hedman, and J. E. Penner-Hahn (Springer, Berlin, 1984), p. 18; K. Zhang, E. A. Stern, J. J. Rehr, and F. Ellis, *Phys. Rev. B* **44**, 2030 (1991).
- [28] W. Malzfeldt, Deutsches Elektronen Synchrotron Hamburg, Report No. DESY F41/HASYLAB, 1985 (unpublished).
- [29] A. Zangwill and P. Soven, *Phys. Rev. A* **21**, 1561 (1980).
- [30] A. Zangwill and D. A. Liberman, *Comput. Phys. Commun.* **32**, 63 (1984).
- [31] D. A. Liberman and A. Zangwill, *Comput. Phys. Commun.* **32**, 75 (1984).
- [32] P. B. Semmes, R. A. Braga, J. C. Griffin, and R. W. Fink, *Phys. Rev. C* **35**, 749 (1987).